Long-term use of modern Portland cement concrete: change in strength due to reaction between aggregate and cement paste

Ippei Maruyama[a,b,*],Abudushalamu Aili[a], Shohei Sawada[c], Kazuhiro Yokokura[d], Yoshito Umeki[e]

a: Graduate School of Environmental Studies, Nagoya University, Nagoya, Japan

b: Graduate School of Engineering, The University of Tokyo, Tokyo, Japan

c: Nuclear Power Department, Kajima Corporation, Tokyo, Japan

d: Civil & Architectural Engineering Department, Hamaoka Nuclear Power Station, Chubu Electric Power Company Incorporated, Shizuoka, Japan

e: Civil & Architectural Engineering Department, Chubu Electric Power Company Incorporated, Nagoya, Japan

[*]: corresponding author, i.maruyama@bme.arch.t.u-tokyo.ac.jp

Abstract

Experimental measurements on samples cored from thick concrete walls of existing building structures whose age was ~50 years at most showed that concrete strength increased after long-term use due to chemical reactions between aggregate and cement hydrates. Chemical compositions of reacted aggregate were analyzed by comparing the oxide composition of cement paste with that of original cement based on inductively coupled plasma atomic emission spectroscopy (ICP-AES) measurement. The results provide indicators to determine the dissolving aggregate minerals as well as the reaction degree of aggregate. A model was proposed to simulate the progress of reaction degree over time in coupling with moisture transport and temperature in concrete. The mechanism of strength increase was discussed by analyzing the gel-space ratio estimated from XRD-Riteveld analysis and that estimated from the thermodynamic simulation of the reaction. Finally, the strength prediction model was proposed for the

aging management of building structures.

Keywords: Concrete (E), Aggregate (D), Reaction (A), Long-term performance (C)

Highlights:

- Minerals dissolving from aggregate were quartz, albite, and chlorite.
- The dissolution rate of aggregate was modeled, considering the coupling with moisture transport in concrete.
- Strength increases due to the reaction between aggregate and cement paste can be regarded as a result of space-filling, i.e., an increase in gel pace ratio.

1 Introduction

The long-term use of concrete structures is one of the significant options to reduce the CO2 emissions from the concrete sector [1]. For this goal, aging management, including structural performance evaluation in the current and future, is necessary. However, the long-term alteration of concrete properties, especially compressive strength, is a significant challenge to predict because there are many scenarios according to the corresponding materials and exposed environments.

The long-term operation of nuclear power plants is also a crucial issue in our society, and carbon neutrality is required to attain a sustainable society. Currently, the building of new-generation nuclear reactors and small modular reactors is under planning, and such a process will take a relatively longer time than that of ordinary structures because of safety regulations and social acceptance. Nuclear energy is considered an important base-load energy in Japan. Therefore, the long-term operation of existing nuclear power plants is promising. Compressive strength is the primary index for the safety evaluation of concrete structures, especially for seismic performance. However, evaluating compressive strength in long-term used concrete members is difficult because of the thickness of the member and different phenomena that affect the compressive strength.

To develop a method to evaluate and predict the compressive strength of the aged

concrete structures exposed to the specific environments of nuclear power plants, we investigated decommissioning plants deeply. During the decommissioning process of the Hamaoka nuclear powerplant in Shizuoka prefecture in Japan, it was found that the strength and Young's modulus of concrete increased after long-term use [2]. In a previous study, it was confirmed that, in unit 1 of the power plant, the aggregates in the concrete dissolved and reacted with hydrates in cement paste based on Rietveld analysis of X-ray diffraction (XRD) data and that the increase of strength was attributed to the "aggregate-paste reaction" [2,3]. The reaction scheme was analyzed using X-ray microdiffraction and energy dissipative X-ray spectroscopy (EDS) to understand the formation of Al-tobermorite (i.e., the crystal form of calcium aluminum silicate hydrates (C-A-S-H)) which was a rare case [4]. Furthermore, similar reactions and strength increases were found to be time-evolving when we analyzed other decommissioning concrete walls constructed at different decades but using aggregates of similar origin. Such field data showing a time-dependent relation of aggregate reaction and compressive strength, measured on harvested samples from real structures with various ages (from ~48 years to ~17 years), cannot be obtained in laboratory experiments and hence precious for long-term performance evaluation of structures. The primary objective of the work is to present these valuable in-situ data and to put forward underlying common phenomena.

Dissolution of aggregate has been studied in the literature in many contexts, such as alkali-silica reaction in cementitious materials [5] and in weathering of rocks in earth science [6]. For main rock-forming minerals found in common aggregates, such as quartz, albite, microcline, and chlorite, the main parameters impacting the dissolution rate are summarized in [7,8] as moisture, temperature, ions in the water, including pH and surface characteristics of the aggregate/mineral such as defects, crystallinity. For the higher range of pH that corresponds to the pore solution in cementitious materials, the effects of temperature, pH, and various ions were systematically studied in laboratory experiments for quartz [9], amorphous silica [10], albite [11], chlorite[12,13] and illite [14]. Experimental data on the long-term dissolution of in-situ aggregates, such as this study, are scarce. Theoretical models accounting for the main factors of dissolution have been established to predict the dissolution rate of minerals and used to estimate stability against weathering [6]. Nevertheless, many complicated phenomena in the dissolution of rock-forming minerals remain to be studied [15]. For instance, the composition of ions released from feldspar during dissolution differs from stoichiometry and is known as incongruent dissolution [16]. Another example of complexity is the formation of a leached layer [15].

Based on these unique field data, the study aims to investigate the underlying common phenomena, i.e., aggregate dissolution, reaction with cement hydrates, and increase of compressive strength. At the same time, the study aims to elucidate the physical mechanism behind the increase in strength and develop a universal methodology for predicting long-term strength that can be promoted for broader use in engineering practice.

The first necessary condition for the dissolution of aggregates in cementitious materials is the pore water, which varies over time due to water transport by advection in liquid form and by diffusion in vapor form. Time evolution of water content in mature concrete can be modeled as a two-phase flow in porous media in a stricter manner [17] but for application in real concrete, simplified models such as the Akita model proposed in [18] can be enough, considering the complexity of boundary condition, variation of microstructure and uncertainty of experimental data caused by coring and measurement techniques. The composition of pore water, including pH values, can be measured experimentally by extracting the pore water [19]. However, due to the difficulty in extracting techniques, they have yet to be widely promoted. As alternatives, thermodynamic simulation of hydration reaction [20,21] and mineralogical analysis of cement hydrates may hint at the pH value. For instance, since portlandite is unstable at a pH lower than 12.5, the presence of portlandite indicates that the pH value of the pore solution is higher than 12.5 [19].

The compressive strength of concrete depends on various factors and is generally related to mixture proportion and microstructure. One of the relevant descriptors of microstructure is gel-space ratio, initially proposed in [22,23] as the volume ratio of amorphous calcium silicate hydrates (C-S-H) to the original space, i.e., the sum of volumes of cement clinker and water. Later, it was found that it is not only the volume of C-S-H gel but the total volume of all hydrates that contributes to the strength development [24]. The definition of gel-space ratio was modified to include the volume of all hydrates, with experimental evidence showing a good relation between such gel-space ratio and the strength of concrete [25–28]. Connecting gel-space ratio to mechanical performance in literature was limited mainly to cement pastes and mortars, even less to concrete with non-reactive aggregate. For the first time, the method will be extended to the case of reacting aggregate to explain the strength increase mechanism in Hamaoka walls.

We start by presenting experimental data from the other three units of the Hamaoka power plan. Then, from the ICP-AES data, we will compute the oxide composition of the

dissolved aggregate. A coupled model of moisture transport and reaction degree will be proposed to understand the reaction rate. The mechanism behind the strength increase will be discussed. We will show how the study's findings can be applied to predict strength evolution over time in plant life management.

2 Material and method

2.1 Samples

Concrete samples were cored from thick concrete walls of the Hamaoka nuclear power plant in the Shizuoka prefecture in Japan, which is now under decommissioning. The power plant comprises five units (H1 to H5), constructed at different times. In this study, we used samples cored from the Biological Shielding Wall (BSW), pedestal (PEDE) and Internal wall 1st floor (IW1-1F) and basement 2nd floor (IW1-B2F) of H2, internal wall (IW1) of H3 and internal wall (IW1) of H5. The coring method is the same as described in [2,29], where samples from BSW, IW1, and PEDE of H1 have been studied. The mixture design of the concrete is listed in Table 1, as well as the age of the concrete at the time when the samples were cored. Table 2 shows the mass of raw materials per unit volume of concrete. The oxide compositions of used cement are shown further in Table 4, together with experimental results to reduce the number of tables.

Table 1 Mixture proportion of concrete for the studied walls

	Age of construction at testing time (years)	Cement type[a]	Design strength (MPa)	Slump (cm)	Air content (%)	Water to cement ratio (%)	Sand volume to aggregate volume ratio (%)
H1-IW1	45	OPC	21	12	3.5	48.3	38.5
H1-BSW	45	MPC	21	12	3.5	48.0	39.7
H1-	45	MPC	21	15	3.5	49.0	42.0

PEDE							
H2	46	MPC	21	12	3.5	48.0	43.0
H3	37	MPC	21	12	3.0	52.0	45.2
H5	20	MPC	21	15	4.0	49.0	45.5

[a]OPC: Ordinary Portland cement; MPC: Moderate heat Portland cement (according to the Japanese Industrial Standard JIS R 5210 [30]).

A schematic representation of the power plant building is shown in Fig. 1 of [2] for H1. The building designs were the same for the other three units in this study. Cylindrical cores were taken from one side of the walls. In the case of BSW and PEDE, the coring was started from the room side (opposite side of the reactor). The water cooling method was used when the core was intended to test strength and phase composition. The dry air-cooling method was also used during coring to test relative humidity. The diameter of the coring was 200 mm. After getting the core, several samples with defined thickness were cut for testing. These samples were noted by the distance between their center and the wall's surface. The thickness of the walls and the number of samples per core are summarized in Table 3.

Table 2 Mass of raw materials per unit volume of mixture (kg/m^3)

	Cement	Water	Water reducing agent	Sand	Gravel
H1-IW1	300	145	2.3	734	1178
H1-BSW	300	144	2.3	758	1160
H1-PEDE	310	152	2.4	792	1096
H2	300	144	3.3	832	1105
H3	288	150	3.0	858	1060
H5	331	162	1.5	822	1004

Table 3 Details of the walls

Target wall	Wall thickness (mm)	Number of samples per core	Surface condition[a]	Temperature during operation (°C)	Temperature after operation (°C)	Duration of operation (years)
H1-IW1	1500	7	N/N	20-30	20-30	16.5
H1-BSW	2200	7	N/L	30-38/50-55	20-30	16.5
H1-PEDE	1220	5	E/E	50-55	20-30	16.5
H2-IW1-1F	1700	7	N/N	20-30	20-30	18.4
H2-IW1-B2F	1700	7	N/N	20-30	20-30	18.4
H2-BSW	2200	7	N/L	30-38/50-55	20-30	18.4
H2-PEDE	1380	5	E/P	50-55	20-30	18.4
H3-IW1	1300	5	N/N	20-30	20-30	18.4
H5-IW1	1000	5	N/N	20-30	20-30	3.1

[a]N: bare surface; L: steel liner; E: epoxy resin coating; P: steel plate.

2.2 Experiments

Multiple experiments were performed to characterize the aged concrete. Here, only the relevant ones are described. It is noted that, as part of the whole project, the experimental methods in this study were the same as those in [2,3].

Compressive strength was measured on samples from wet coring. Cylindrical samples of size φ200 mm × 100 mm were polished and measured according to the Japanese Industrial Standard JIS A 1149 [31].

Water content was measured using samples from dry coring. Approximately 1500 g of sample was roughly crushed into particles of size 10-20 mm and then dried at 105 °C until a constant mass was reached while a 100 mL/min nitrogen gas flow passed through during the whole heating. Water content was obtained by taking the mass loss as the mass of evaporable water in the sample and normalizing it with the mass of the sample after heating at 105 °C.

Relative humidity at the coring time was measured using samples from dry coring. The samples were sealed immediately after coring and shipped to the constant temperature room at 20 ± 0.2 °C, where around 10 g samples were chipped from inside the portion. Then, the chipped block was sealed in an aluminum-coated polyvinyl bag, roughly crushed, and put inside a water activity meter (AQUALAB 4TE, METER Group) to measure the relative humidity.

Total porosity was measured using samples from wet coring. Samples of size φ200 mm ×100 mm were immersed in water and vacuumed for one hour. Then, the samples remained in water while the mass was measured every 24 hours. When the difference between the two subsequent measurements was less than 0.1 g, the samples were considered fully saturated, and saturated mass was noted. The apparent volume of the sample was measured using the Archimedes method. Finally, we obtained the dry mass by drying the sample at 105 °C with a 100 mL/min nitrogen gas flow. Taking the difference between saturated and dry mass as the mass of water filling all the pores, we obtained the total volume of the pores and normalized to the apparent volume of the sample.

Quantitative X-ray diffraction (Q-XRD) was measured using samples from wet coring. Samples were roughly crushed into sizes less than 5 mm, and visible aggregates larger than 3 mm were removed. The remaining part was considered mortar and ground into a fine powder of less than 90 µm particle size. The objective was to determine the phases

in the cement paste; preparing such mortar by removing big aggregates was considered valid. The fine powder was dried at a relative humidity of 11% for two weeks and then mixed with a 10% mass of corundum as an internal reference. X-ray diffraction profiles were measured between 2θ=2-65°, using three replicates for each sample. The diffraction patterns of H2-IW1-1F&B2F, H2-PEDE, H3-IW1, and H5-IW1 were measured by a D8 ADVANCE (Bruker AXS) that uses a Cu-Kα X-Ray source at 40 kV and 40 mA, in increments of 0.02°, with a speed of 0.5°/min. For H2-BSW, the diffraction patterns were measured by a PANalytical Empyrean diffractometer (Malvern PANalytical) that uses a Cu-Kα X-Ray source at 45 kV and 40 mA, in increments of 0.026°, with a speed of 300 s/step.

Inductively coupled plasma atomic emission spectroscopy (ICP-AES) was measured using the same mortar powder samples as Q-XRD. In the first step, around 1 g of mortar powder sample was put in hydrochloride acid solution (1.65 mol/L) and stirred for 30 minutes. Then, the insoluble residue was filtered out while the solution was collected (noted as solution 1). In the second step, the filtered insoluble residue was put in potassium hydroxide solution (0.2 mol/L) and left at 70 °C for 60 minutes. Again, the solution was collected (noted as solution 2) while the insoluble solid was filtered out. In the third step, on the one hand, the final residue was heated at 1000 °C for 60 minutes to obtain the mass of the insoluble part of the initial mortar sample. On the other hand, analyzing solutions 1 and 2 by ICP-AES, the oxide compositions (CaO, SiO_2, Al_2O_3, Fe_2O_3, MgO, SO_3, Na_2O, and K_2O) of soluble part of the mortar sample were obtained. The difference, obtained by subtracting the sum of the oxides' mass and the insoluble mass from the initial mass of the mortar sample, was considered as the sum of loss on ignition (OH^- and CO_3^{2-}) and of other minor elements.

Similar dissolution processes in solutions 1 and 2 were performed on fine aggregates, yielding the oxide composition of the soluble part of the aggregate and the insoluble mass.

3 Experimental results

3.1 Compressive strength, water content, relative humidity, and total porosity

The strength of cores is displayed in Figure 1 in the function of core position, which is defined as a linear transformation of the distance between the core center and wall surface. In this linear transformation, the center of the core is noted as 0, and the outer and inner surfaces as -1 and +1, respectively. The compressive strength is higher than the designed strength of 21 MPa and even increased further in the inner parts to surpass

the potential strength of 40 MPa expected at 91 days. In the IW1s, which were submitted to a constant temperature of 25 °C since the construction, the profile of compressive strength along the wall thickness is a convex shape (see Figure 1a), whereas, in BSW and PEDE with high-temperature history, increase of compressive strength is more significant towards the inner part where the temperature during operation was high.

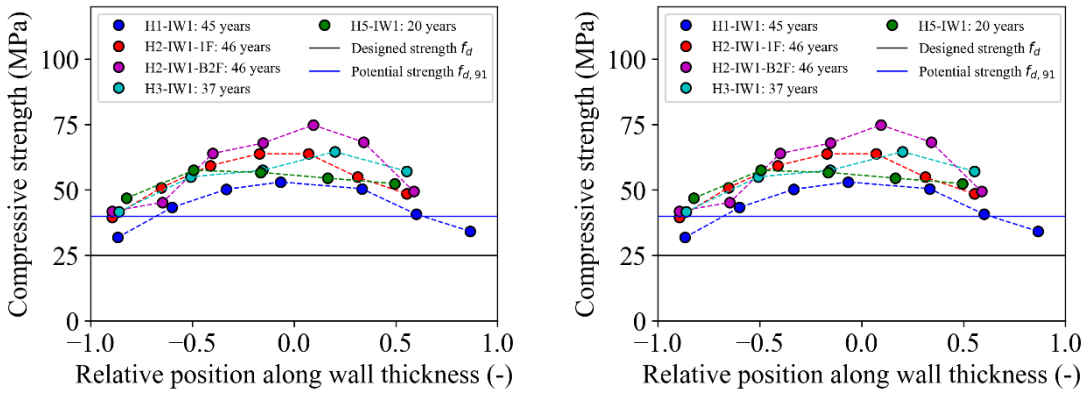

Figure 1 Compressive strength versus the core position along the wall thickness. X-axis 0 represents the wall center, while ±1 represents the two surfaces. (a) internal walls without high-temperature history; (b) BSWs and PEDEs with high-temperature history.

The results of water content and relative humidity measurement are shown in Figure 2. Like the strength profile, a convex shape was shown in water content and relative humidity of IW1s. The water content of H1 was significantly lower than other IW1s. At the same time, the relative humidity was similar to that of other IW1, indicating a fundamental difference between H1-IW1 and all other IW1: H1-IW1 was OPC, whereas all other walls were composed of MPC. The OPC concrete has higher water diffusivity than MPC concrete due to its higher calcium content in the main hydrate phase C-S-H, through which the water diffuses. The water content of IW1 of H2, H3, and H5 were similar despite the age difference (see Table 1).

Nevertheless, this similarity can be explained by the difference in thickness. Taking the half thickness of the wall as the diffusion length and considering the same diffusion coefficients, the ratio of the characteristic diffusion times in H2 and H5 would be 2.9. The 16-year age in H5-IW1 is equivalent to 46 years in H2-IW1.

In BSWs, water content and relative humidity were lower near the outer surface (position -1 in Figure 2b and d), which was not coated. Thanks to the metallic liner, the water content and relative humidity were kept higher towards the inner surface (position 1 in Figure 2b and d). The water content profile and relative humidity PEDEs were consistent with their corresponding coating conditions.

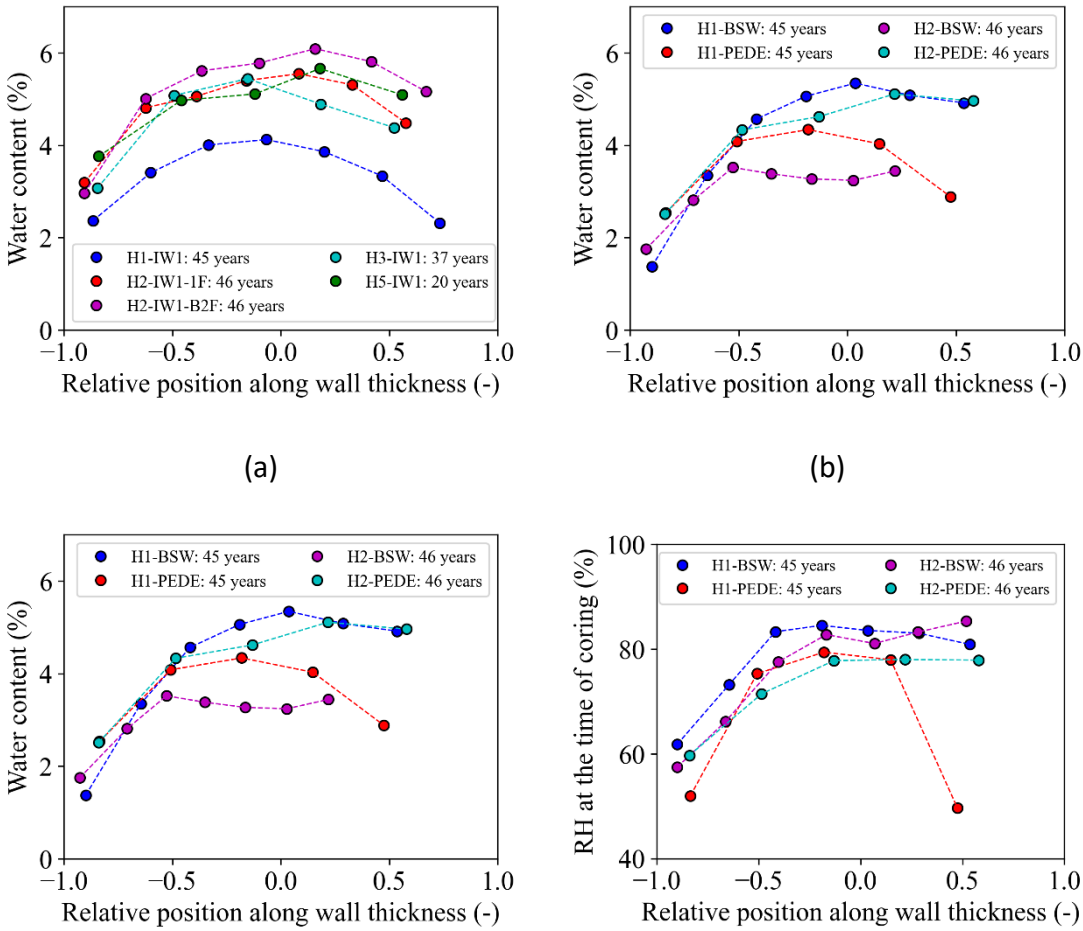

(a) (b)

(c) (d)

Figure 2 Water content and relative humidity versus core position along the wall thickness. X-axis 0 represents the wall center, while ±1 represents the two surfaces. (a)(c): IW1s without high-temperature history; (b)(d): BSWs and PEDEs with high-temperature history.

The results of the porosity measurement are shown in Appendix A, Figure A1. In contrast

to water content, the porosity did not show any clear trend along the wall thickness but was approximately constant. We attribute the quasi-uniform porosity to the same mixture proportion and similar hydration degree along the wall thickness, which was confirmed by the XRD results in the next section.

3.2 XRD results

XRD diffraction patterns were analyzed using the Rietveld method following the protocol established in [26] and using the same phases listed in [4], given the same origin of aggregate. From the obtained phase compositions of each core position, aggregate minerals (i.e., quartz, albite, muscovite, chlorite, illite, biotite, and microcline) were excluded to obtain the phase composition of cement paste only. Similar to the findings in H1 shown in [2], portlandite was absent in the inner part of the walls where water content was relatively high. The crystal form of C-A-S-H, Al-tobermorite was observed in H2-PEDE, in addition to H1-BSW and PEDE. The decrease in portlandite was consistent with the increase of amorphous content in IW1s, as shown in Figure 3a and c. In Figure 3b and d of BSW and PEDE, the sum of amorphous content and Al-tobermorite was inversely correlated to portlandite. Unreacted cement clinker phases were approximately uniform along the depth of each wall.

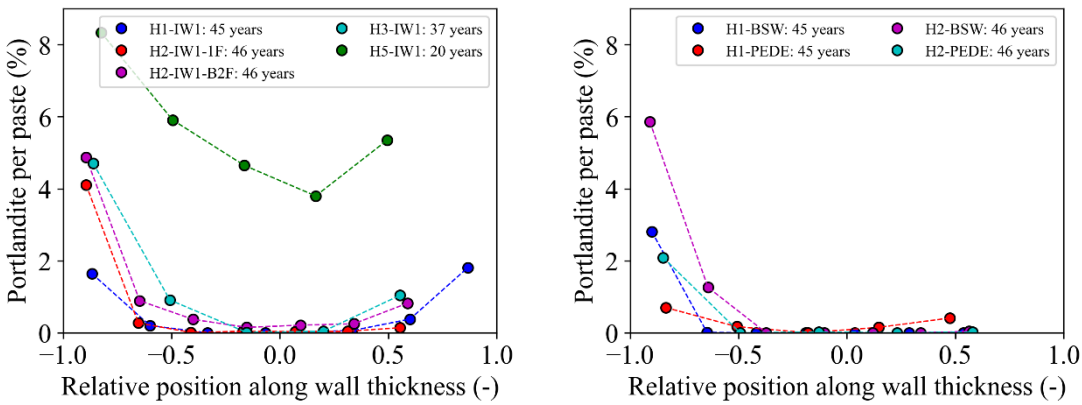

(a) (b)

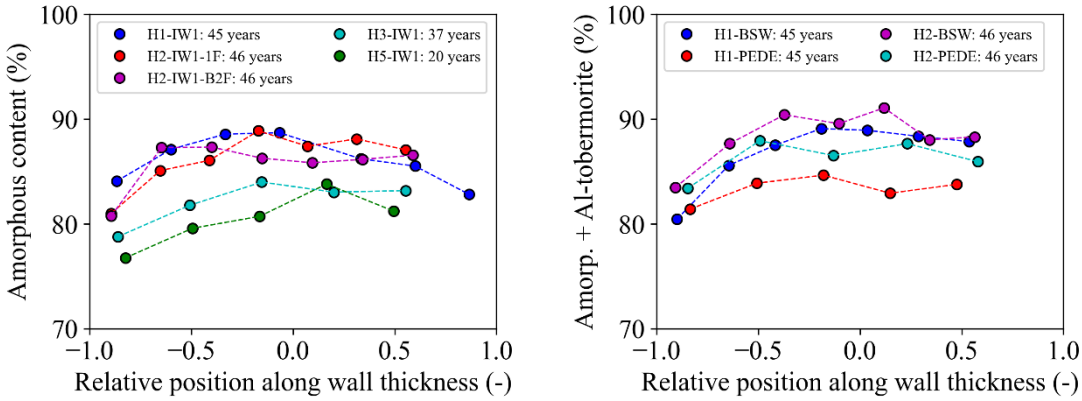

(c) (d)

Figure 3 Portlandite and the sum of amorphous phase and Al-tobermorite content in the cement paste versus core position. X-axis 0 represents the wall center while ±1 represents the two surfaces. (a)(c): IW1s without high-temperature history; (b)(d): BSWs and PEDEs with high-temperature history.

3.3 ICP-AES

In the ICP-AES measurement, we obtained the oxide composition $m_i^{diss,m}$ (i =CaO, SiO_2, Al_2O_3, Fe_2O_3, MgO, SO_3, Na_2O, and K_2O) of soluble part, insoluble mass, and mass of ignition loss for mortar sample at each coring position for each wall, as well as for sound fine aggregate. Assuming that the insoluble part of mortar is from fine aggregate only, the dissolved oxides $m_i^{diss,a}$ from aggregate, was estimated. Subtracting $m_i^{diss,a}$ from the total dissolved oxides, we obtained the oxide composition of the cement paste part: $m_i^p = m_i^{diss,m} - m_i^{diss,a}$. Significant differences between this oxide composition m_i^p and the oxide composition of the original OPC/MPC in Table 4 confirmed the dissolution of some aggregates into the paste, hence the aggregate-paste reaction.

Table 4 Oxide compositions of Ordinary Portland cement, Moderate heat Portland cement, and cement paste part from three walls for comparison.

Oxide	CaO	SiO_2	Al_2O_3	Fe_2O_3	MgO	SO_3	Na_2O	K_2O	Sum
OPC	65.37	22.13	5.25	3.23	1.62	1.72	0.28	0.40	100

MPC	64.51	23.68	3.84	3.93	1.10	2.27	0.26	0.40	100
H2-BSW-690	51.94	35.59	5.00	4.05	1.14	1.37	0.64	0.27	100
H3-IW1-550	53.73	33.27	5.20	3.59	1.58	1.80	0.50	0.33	100
H5-IW1-252.5	58.67	29.94	4.43	3.60	1.15	1.81	0.25	0.15	100

We assumed that all the calcium oxide in the cement paste part m_i^p originated from the original OPC/MPC. Comparing the mass fraction m_{CaO}^p of calcium oxide in the cement paste part with m_{CaO}^{OPC} or m_{CaO}^{MPC} in the OPC/MPC, the mass fraction φ_a of oxides originating from the dissolved aggregate was estimated. Then, the reaction degree of aggregate ζ, i.e., the mass ratio of the reacted aggregate over the initial aggregate, was calculated by:

$$\zeta = \frac{\varphi_a}{a/c} = \frac{m_{CaO}^{MPC} - m_{CaO}^p}{m_{CaO}^p} \frac{1}{a/c}, \quad (1)$$

with a/c as the aggregate-to-cement mass ratio from the initial mixture proportion.

The obtained reaction degree of aggregates is displayed in Figure 4 as a function of the relative position of the cores along the wall thickness. The results show that the reaction degree of aggregate evolves with time, showing a higher reaction degree in H1 and H2, whose construction ages were ~46 years, than in the other units, H3 and H5. For each wall, the reaction degree is higher in the inner part than in the parts near the surface, indicating that water content and relative humidity are necessary conditions for the aggregate reaction. In H1 and H2, the walls that experienced high temperatures during the power plant's operation (i.e., BSW and IW1) showed higher reaction degrees, which the thermal activation of the reaction can explain. The lower reaction degree in H2-BSW,

when compared with that in H1-BSW, is likely attributed to the longer high temperature in H2. Due to the longer duration of higher temperatures, drying could be accelerated, resulting in less water and a lower reaction degree in H2-BSW.

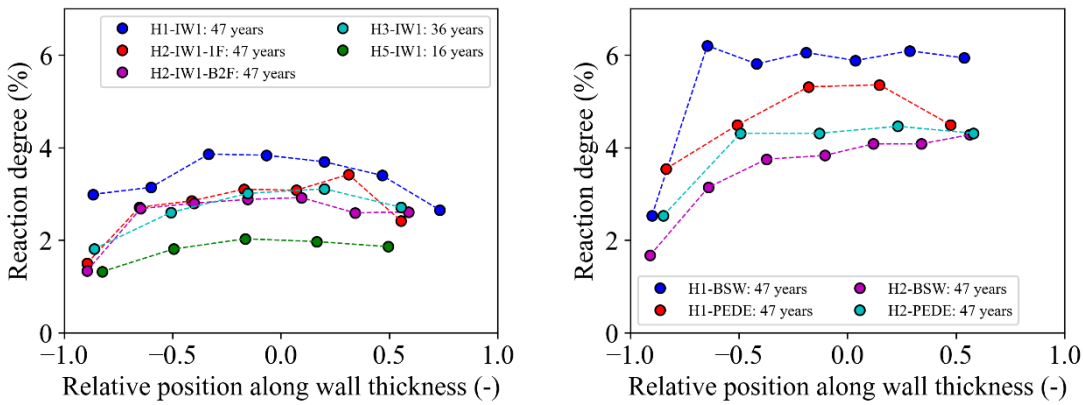

(a) (b)

Figure 4 Reaction degree of aggregate versus core position. X-axis 0 represents the wall center, while ±1 represents the two surfaces. (a): IW1s without high-temperature history; (b): BSWs and PEDEs with high-temperature history.

For example, the reaction degree of 3.1% in the center of H2-IW1-1F indicates that 26 kg aggregates dissolved and reacted in 1 m^3 of concrete, increasing 39 MPa of compressive strength compared to the designed strength of 25 MPa. It is even more significant for walls with a high-temperature history. For instance, the reaction degree of 6.2% in H1-BSW implies a reaction of 47 kg aggregates per m^3 of concrete and an increase of compressive strength by 47 MPa. Therefore, the aggregate-paste reaction and its contribution to the strength increase are significant. Clarifying reaction kinetics and strength increase mechanisms are helpful for the aging management of thick concrete walls.

4 Analysis of the aggregate-paste reaction

The reaction between aggregate and cement hydrates happened in all the walls and showed time-dependent characteristics, as shown in section 3.3. Even though those walls were constructed in different decades, aggregates from the same origin were used.

Therefore, we believe that the reaction in these walls is a universal phenomenon and that the reaction scheme and kinetics are worth investigating and can be extrapolated to broader applications. In the first part of this section, the oxide composition of dissolved aggregate will be deduced from ICP-AES results to infer the reacting minerals of the aggregate. In the second part, we aim to understand the time evolution of the aggregate-paste reaction, considering given temperature and moisture conditions.

4.1 Composition of dissolved-reacted aggregate

Reacted aggregates were identifiable from the texture in backscattered electron (BSE) images in previous studies, such as Figure 5a, measured in [2]. Moreover, the EDS maps measured in [4] showed silica released from sandstone aggregates (see Si-Map in Figure 5b). On the other hand, the mineral composition of the aggregates has been studied extensively in [3,32], whose results are summarized in Table 5. To clarify which of these rock-forming minerals dissolved and reacted, the oxide composition of the dissolved part needs to be analyzed quantitatively first.

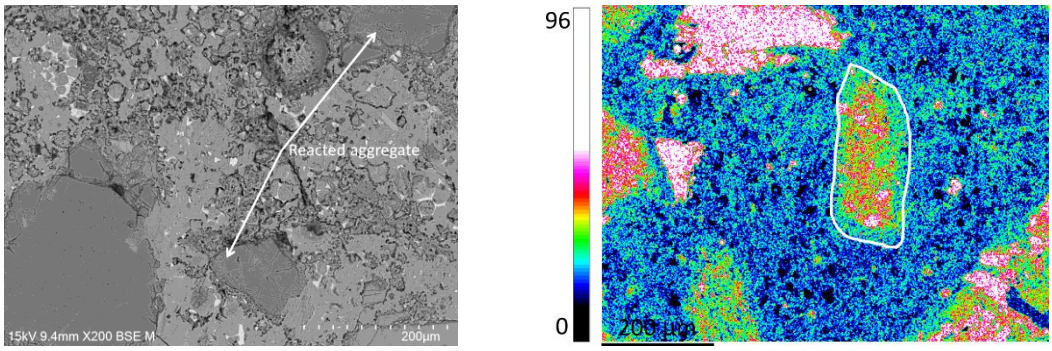

(a) (b)

Figure 5 Identifiable reacted aggregates: (a) BSE image retrieved from [2]; (b) Si map from EDS measurement retrieved from [4].

For oxide i (where i= SiO_2, Al_2O_3, Fe_2O_3, MgO, SO_3, Na_2O, and K_2O), using the ratio $m_{CaO}^{p}/m_{CaO}^{MPC}$ of the calcium oxide in the cement paste to that in the original MPC (same procedure for OPC system), the mass originating from the initial MPC was estimated. Then, subtracting this mass from the total mass m_i^p of the oxide i in the cement paste, the mass w_i^{agg} from the dissolved aggregate is computed:

$$w_i^{agg} = m_i^p - m_i^{MPC} \frac{m_{CaO}^p}{m_{CaO}^{MPC}}. \quad (2)$$

Neglecting the oxides whose mass is less than 1% and normalizing to 100%, the oxide compositions of dissolved aggregate were obtained for each core sample. The results of dissolved aggregate composition for each core are listed in Table B1 of Appendix B. Figure 6a shows the compositions of dissolved aggregate per wall, including the three walls from H1. The compositions of dissolved aggregate are not the same in all walls but can be categorized into three main types:

- General case excluding H1-IW1 and H1-BSW, composed approximately from ~85% of SiO_2, ~9% of Al_2O_3, ~3% of Fe_2O_3 and of minor amount of MgO and Na_2O.
- Case of OPC system for H1-IW1: compared with the general case, does not contain MgO.
- Case of H1-BSW: compared with the general case, does not contain MgO but K_2O.

Table 5 Mineral composition of aggregates (retrieved from [3,32])

Mineral name	Chemical formula
Quartz	SiO_2
Albite	$NaAlSi_3O_8$
Microcline	$KAlSi_3O_8$
Muscovite	$KAl_2(AlSi_3O_{10})(F,OH)_2$
Chlorite	$(Mg,Fe)_3(Si,Al)_4O_{10}(OH)_2 \cdot (Mg,Fe)_3(OH)_6$
Illite	$(K,H_3O)(Al,Mg,Fe)_2(Si,Al)_4O_{10}[(OH)_2,(H_2O)]$
Biotite	$K(Mg,Fe)_3(AlSi_3O_{10})(F,OH)_2$

Since SiO_2 is the dominant oxide in all cases, it can be inferred that quartz is the main

dissolving mineral. The presence of Na indicates that albite dissolved in all the walls; meanwhile, from the same feldspar group, microcline and muscovite dissolved only in H1-BSW. From Fe and Mg content, it is deduced that chlorite was also dissolving in all the walls. It is also possible that the incongruent dissolution of feldspar minerals resulted in high silica content in the dissolved oxides.

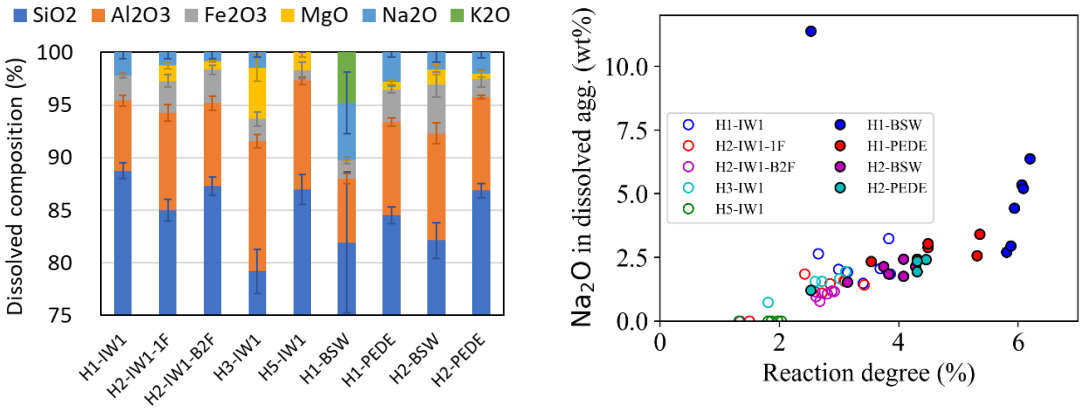

(a) (b)

Figure 6 (a) Composition of dissolved aggregate averaged per wall. Error bar is the standard deviation of all the samples of the same wall; (b) Na_2O fraction in dissolved aggregate versus reaction degree.

The variation of dissolved aggregate composition over time can be inferred by comparing the oxide composition at different reaction degrees. The percentages of SiO_2, Al_2O_3, and Fe_2O_3 in dissolved components did not show any trend with the reaction degree of aggregate. As shown in Figure 6b, Na_2O increased with the increase of reaction degree, suggesting that albite may have dissolved more at later stages.

4.2 Time evolution of reaction degree

Given the reaction degree in walls of different ages in Figure 4, this section proposes a model for the time evolution of the aggregate-paste reaction. Since the reaction was confirmed to be a dissolution-precipitation process in [4], the main factors influencing the reaction rate would be evaporable content, temperature, and pH values. The

measured reaction degrees are plotted in function of water content for different temperature histories in Figure 7a, showing the role of water content and temperature respectively: i) Higher water content corresponds to a higher reaction degree; ii) In walls without high-temperature history, the reaction degree reached only 3.4%, whereas for walls with high-temperature history, the majority of the cores showed a higher reaction degree than 3.4%. Due to a lack of measurement and estimation methods, the impact of the pH will not be considered in the following.

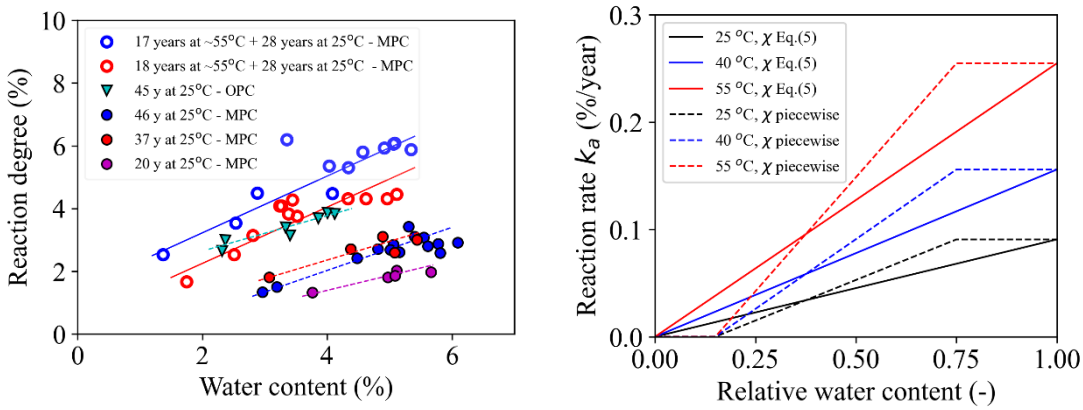

(a) (b)

Figure 7 (a) Measured reaction degree versus age of walls, water content, and temperature history. (b) Proposed model for reaction rate depending on relative water content and temperature.

Hence, it is necessary to know water content $w(t)$ to predict the time evolution of reaction degree $\zeta(t)$. Water content changes are controlled by two phenomena: moisture transport and water consumption by aggregate-paste reaction. Reduction in water content slows down the aggregate-paste reaction, whereas the progress of the reaction makes the moisture transport more difficult by densifying the microstructure. These couplings between water transport and aggregate-paste reaction are shown in Figure 9. The model is written as two coupled equations:

$$\frac{\partial w}{\partial t} = \frac{\partial}{\partial x} D(w) \frac{\partial w}{\partial x} - \theta \frac{\mathrm{d}\zeta}{\mathrm{d}t}, \tag{3}$$

$$\zeta = \int_0^t k_a(T, w) \mathrm{d}t. \tag{4}$$

with D, θ, k_a diffusion coefficient (m^2/s), the ratio of reacted aggregate and consumed water, and the dissolution rate of aggregate, respectively. Coupled solution of Eqs. (3) and (4) will result in time-evolution of water content and reaction degree. The input parameters of the model are explained below.

Eq.(3) is based on a developed version of the Akita model [33,34], which related $D(w)$ to water content-dependent permeability $K(w)$ ($m^2/s \cdot g/m^3 \cdot (J/g)^{-1}$) via

$$D(w, T) = \alpha K(w) \frac{p_{sat}(T)}{p_{sat}(T_0)} \frac{\partial \mu}{\partial w} = \alpha \frac{K_{60}}{5 - 9.1\chi + 4.15\chi^2} \frac{p_{sat}(T)}{p_{sat}(T_0)} \frac{\partial \mu}{\partial w}. \tag{5}$$

In Eq.(5), K_{60} is the reference permeability at a water content of 60%, obtained from the empirical relation in the same reference [33], and equal to 4.25×10^{-7} m^2/s. The term $\partial \mu / \partial w$ represents the change of water chemical potential μ (J/g) with respect to the change of water content, and its value has been fitted to be 0.0026 J/g for the cement paste of water-to-cement ratio 0.55 of MPC system in Table 2 of [34]. Term $p_{sat}(T)/p_{sat}(T_0)$ accounts for the impact of temperature on moisture transport kinetics, with $p_{sat}(T)$ representing the saturated vapor pressure of water at temperature T. In contrast to a constant value in [33,34], α is supposed to depend on the reaction degree to take into account the impact of the reaction on water transport,

$$\alpha = \alpha(\zeta) = \alpha_0 10^{-\beta\zeta}, \tag{6}$$

with α_0 reference value for the concrete without aggregate-paste reaction, β reduction factor due to aggregate-paste reaction.

Regarding aggregate-paste reaction, the dissolution rate of aggregate k_a depends on

temperature T and water content w as seen in Figure 7a, thus can be written as $k_a(T,w) = k(T)\chi(w)$, with $k(T)$ and $\chi(w)$ are the functions to account for the impact of temperature and water content, respectively. The term $k(T)$ accounting temperature impact is considered similar to the Arrhenius equation, i.e.:

$$k(T) = A\exp\left(-\frac{E_a}{RT}\right), \tag{7}$$

where A is a constant (%/year), E_a is the activation energy (J/mol), and R is the universal gas constant (8.314 J/mol/K).

About the function $\chi(w)$ role of water content, the straightforward choice with the least parameters is the relative water content:

$$\chi(w) = \frac{w}{w_{sat}}, \tag{8}$$

with w_{sat} the saturated water content, which is estimated from the measured total porosity. The reaction rate k_a obtained by a combination of Eqs.(7) and (8) is shown in Figure 7b for three different temperatures. It should be noted that the horizontal axis in Figure 7a is the water content at the end of the reaction, whereas it is the actual water content during reaction time. Similarly, the vertical axis is the reaction degree and rate, respectively, in Figure 7a and Figure 7b.

Both water transport and aggregate-paste reaction depend on the temperature. The temperature history $T(t)$ can be estimated according to Table 3 from the power plants' operation time: for IW1 in all four units, the temperature was constant at 25 °C. For BSWs and PEDEs, during the period of operation, the temperature was considered linearly distributed along the thickness of the wall and constant over time, as shown in Figure 8. For the following period, during which the power plants were shut off, the temperature was considered equal to 25 °C. Note that the temperatures listed in Table 3 were based on measurement, but the details of measurement and results were not revealed to the authors for confidentiality reasons.

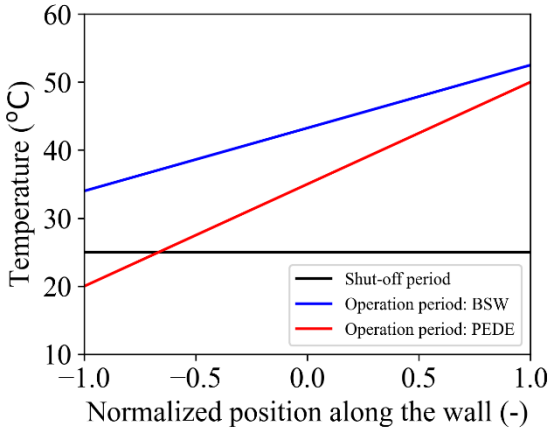

Figure 8 History of temperature distribution in BSW and PEDE of H1 and H2.

Input parameters of the FDM simulations include: i) initial conditions (i.e., initial water content) were based on measurement results in Figure 2; ii) boundary conditions were chosen to be Neuman boundary conditions, with the value of derivate depending on the surface coating conditions of the wall, as listed in Table 6. iii) reference permeability K_{60} =4.25×10^{-7} m^2/s; iv) five other fitting parameters: $\alpha_0, \beta, \theta, E_a$, and A. By varying these five parameters, it is possible to obtain multiple combinations that give the best fit of the experimental results of water content and reaction degree. Nevertheless, such combinations lack physical meaning and applicability. Instead, the following strategy was adopted to retrieve meaningful conclusions.

Table 6 Boundary condition in the FDM simulations

Surface condition	Derivative [m^{-1}]
No coating	0.12
Epoxy	0.09
Metallic liner	0.02
Steel plate	0.02

Firstly, since the concrete mixture compositions and total porosity of the walls are similar, the value of α_0 is fixed to be 0.1 for all walls. Secondly, the value of θ is set to be 0.1 based on a preliminary study by many simulations. Thirdly, various combinations of E_a and A may give the same results; hence, it was decided to fix the value of E_a to 28 kJ/mol to be consistent with the previous work [2]. Consequently, only β and A are changed to obtain the profile of water content and the profile of reaction degree that best fits the measured results. The flow chart of the combined FDM solution of Eqs.(3) and (4) is shown in Figure 9, with a recapitulation of the model's fixed and fitting parameters.

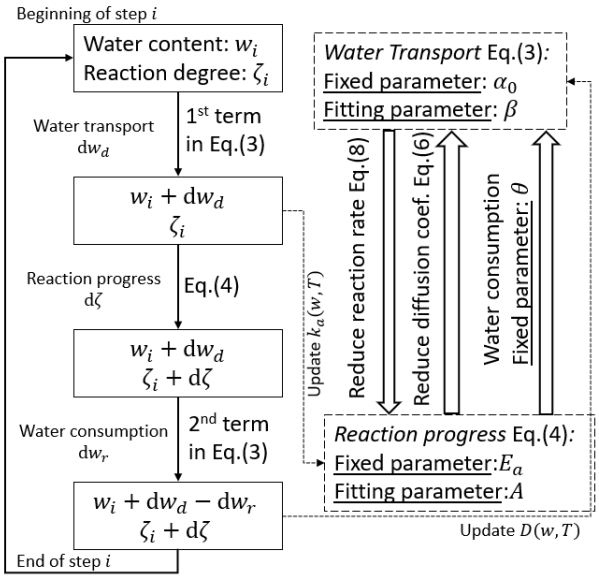

Figure 9 Interaction between moisture transport and reaction; flow chart of FDM solution of the model

The values of fitting parameters are summarized in Table 7, while the simulation results are compared with experimental results in Figure 10.

Table 7 Summary of fitting results of moisture transport and reaction degree model.

Without high-temperature history	With high-temperature history

Walls	β (-)	$k(20°C)$[a] (%/year)	Walls	β (-)	$k(20°C)$ (%/year)
α_0=0.1, θ=0.1, E_a=28 kJ/mol					
H1-IW1	10	0.086	H1-BSW	20	0.094
H2-IW1	100	0.056	H1-PEDE	20	0.108
H3-IW1	100	0.079	H2-BSW	20	0.064
H5-IW1	100	0.108	H2-PEDE	50	0.075

[a]For ease of understanding physical meaning, reaction rate $k(20°C)$ is given instead of A. The relation between A and $k(20°C)$ is shown in Eq.(7).

The reduction factor β was equal to 100 for all IW1s made with MPC (i.e., H2, H3, and H5). In walls with high-temperature history, β was equal to 50 for three walls except from H2-PEDE. Hence, we infer that the aggregate-paste reaction similarly reduced the water diffusion coefficient in all MPC systems and that such reduction impact is less significant at higher temperatures. In the OPC system of H1-IW1, the reduction seems even less severe.

The reaction rate $k(20°C)$ of aggregates was not equal for all walls but higher for younger walls than older ones. One of the reasons for faster kinetics in younger walls might be the choice of $\chi = w/w_{sat}$, which implies that the reaction rate decreases linearly proportional to the decrease of water content. It is plausible that below a certain water content, $w_{cr,l}$, aggregate minerals cannot dissolve any more, and the reaction ceases. Similarly, for water content above a certain level of $w_{cr,u}$, the water content may not impact the dissolution rate. From Figure 7a, we may deduce that $w_{cr,l}$=1%, $w_{cr,u}$=5% for IW1s, and $w_{cr,l}$=0, $w_{cr,u}$=4% for BSWs and PEDEs. By choosing a piecewise function for χ (1 for $w > w_{cr,l}$,0 for $w < w_{cr,0}$ and linear function in between, shown in dashed lines in Figure 7b), we have solved Eqs.(4) and (3). The shape of the obtained reaction degree profile does not match the measured results. Adjusting values of $w_{cr,l}$ and $w_{cr,u}$, and choosing another function shape rather than linear, we might get better fitting, but it would let the model look like curve-fitting.

Another possible reason for the difference in reaction rate between walls could be the

change in pH. Though no pH data is available in this study, it is known that the dissolution of SiO_2 and alkali oxides reduces the pH value of the pore solution. The disappearance of portlandite also supports the decrease in pH. As shown in [8], decreasing pH from 13 to 12 reduced the release rates of SiO_2 from quartz and albite by almost half. Thus, it is reasonable to assume that the reaction becomes slower with the progress of the reaction.

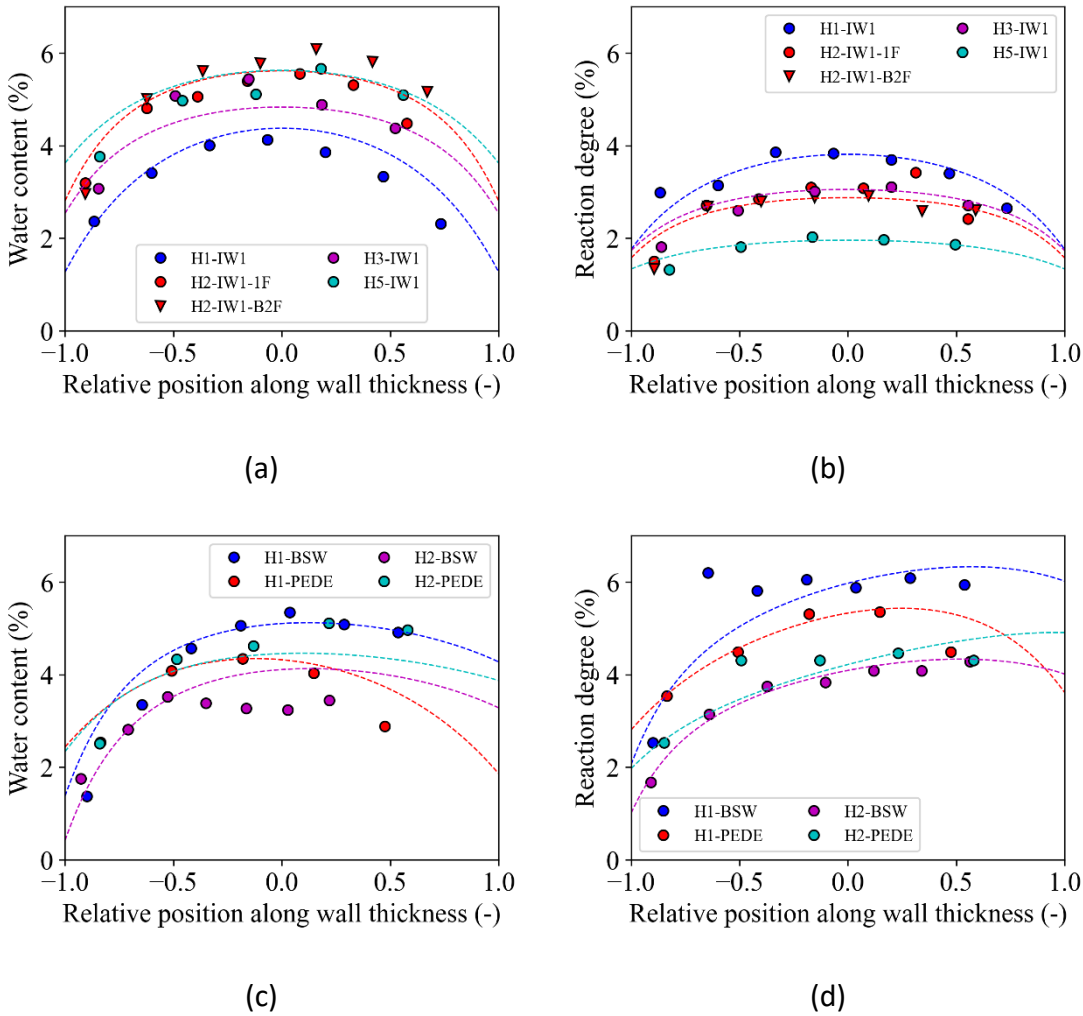

Figure 10 Results of simulation compared with measurement, (a)(c) water content and (b)(d) reaction degree. Points are experimental results; dashed lines are simulation results. The color of the dashed lines represents the simulated wall.

5 Mechanism of strength increase

Since the measured porosity (see Figure A1 in the appendix) is approximately constant and does not show any clear trend with regard to the core position, the increase of compressive strength in the center cannot be explained simply by porosity. Instead, the compressive strength is correlated with the reaction degree, as shown in Figure 11. Despite the difference in the age of construction between different walls, compressive strength and reaction degree show a single relationship for all walls without high-temperature history, i.e., IW1s. Another single relation is also seen for walls with high-temperature exposure (i.e., BSW and PEDE), in which a higher reaction degree corresponds to the same compressive strength in IW1s. Therefore, the reaction degree and temperature history can be considered the main factors explaining the increase of compressive strength in these walls.

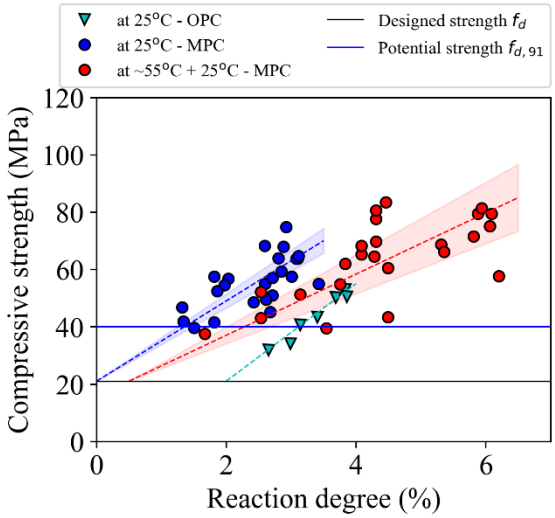

Figure 11 Correlation between compressive strength and reaction degree. The shaded areas represent prediction using a 95% confidence interval for the slope of best fit, blue for walls without high temperature, and red for walls with high-temperature history.

For the mechanism of strength increase due to aggregate-paste reaction, we assume that the reaction increased the gel-space ratio. By filling the space more efficiently with the reaction product, an increase in reaction degree resulted in a higher strength.

Concerning the temperature, the impact of high temperature is twofold: on the one hand, higher temperature increases reaction degree by accelerating aggregate dissolution. On the other hand, an increase in temperature might have caused: i) coarsening of amorphous C-A-S-H agglomeration; ii) different thermal strains in aggregate and cement paste resulting in volume mismatch and hence cracks [35–45]. These two phenomena also explain the lower reduction factor β for BSWs and PEDEs in Table 7. The reduction effect of these two phenomena explains why the $f_c \sim \zeta$ line for walls with high-temperature history lies below that for walls without high-temperature history in Figure 11.

The following part of the section is dedicated to supporting the hypothesis on the role of aggregate-paste reaction by evaluating the gel-space ratio of the samples. Two methods are applied.

The first method was based on the XRD-Rietveld analysis, from which the mass of cement hydrates and amorphous phases were known. The volume V_g of the reaction product (i.e., all hydrates) was computed as the sum of cement hydrate minerals and amorphous phase volumes. The density of cement hydrate minerals and amorphous phase is listed in Table 8. Considering the theoretical ignited mass of minerals and amorphous phase equal to the sum of the mass of reacted cement clinker and reacted aggregate, we obtained the sum of the mass of reacted aggregate and reacted clinker. Then, combined with the reaction degree, we obtained the mass of the reacted aggregate and reacted clinker, respectively. The sum of the volume of these two and of water was computed as the volume V_s of initial space. Then, the gel-space ratio g/s was obtained from:

$$\frac{g}{s} = \frac{V_g}{V_s}. \tag{9}$$

Regarding the second method, the aggregate-paste reaction was first simulated using the software GEMS[46,47] (https://gems.web.psi.ch), which is widely used for the thermodynamic simulation of chemical reactions in cementitious materials. The input reactants were MPC, water, and dissolved aggregate composition based on ICP-AES results. The CSHQ model from database Cemdata18 [21] was used in the simulation, noting that no C-S-H model in the database of GEMS includes Al-tobermorite. Then, the

volume V_g was computed as the sum of solid reaction products, whereas the space volume V_s was estimated using the density data in Table 8. Finally, inserting V_g and V_s into Eq.(9), the gel-space ratio is computed.

Table 8 shows the Density of cement hydrates, cement clinker, and aggregate used to estimate the gel-space ratio from XRD results, in g/cm^3.

Amorphous	Al-Tobermorite	Portlandite	Ettringite	Hydrogarnet	Monosulphate	Monocarbonate	Hemicarbonaluminate	Calcite	Clinker	aggregate
2.3	2.45	2.24	2.38	2.52	2.4	2.4	2.4	2.7	3.15	2.65

The reaction products obtained in GEMS simulations differ slightly from the XRD measurement. For instance, in H1-IW1, portlandite was still present in the inner part of the wall, whereas XRD measurements show no portlandite remained. Another difference is that, with respect to the total volume of reaction products, the amorphous phase in XRD results accounts for more fraction than the CSHQ phase in GEMS results. One of the probable explanations could be that the reaction products in real structures were in an unsteady state and had not yet reached thermodynamic equilibrium and hence contained more amorphous. In contrast, the GEMS simulates a thermodynamic equilibrium state.

The gel-space ratios obtained from the two methods are compared in Figure 12a. For IW1s made with MPC, the gel-space ratio obtained from GEMS is higher than that obtained from XRD. On the contrary, for BSW, PEDEs, and H1-IW1, GEMS simulations result in a lower gel-space ratio than that from XRD results. Such a difference might be correlated to the temperature hist

ory. The gel-space ratios from XRD-Rietveld analysis are affected by the real temperature history under which aggregate-paste reaction progressed gradually over decades. In contrast, in the GEMS simulation, the reaction temperature was set to 20 °C, and the reaction happened as an instantaneous process.

Nevertheless, despite such differences in reaction conditions, both XRD results and

GEMS simulations show an increasing trend in the gel-space ratio with the progress of the reaction.

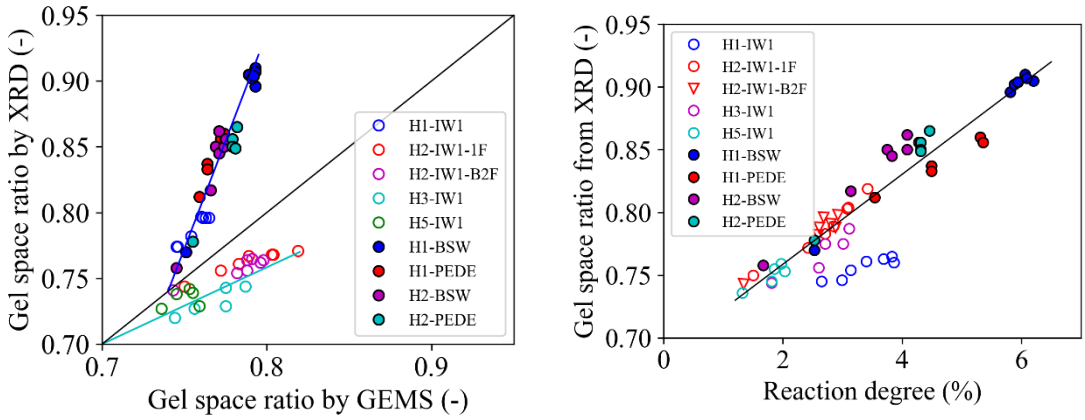

(a) (b)

Figure 12 (a) Comparison of gel-space ratio calculated from XRD results and GEMS simulations. (b) Gel-space ratio versus Reaction degree.

The estimated gel-space ratios from XRD results are shown as a function of reaction degree in Figure 12b. For all the walls made with MPC, the gel-space ratio g/s is almost linearly correlated with the reaction degree. In the case of the OPC system, the gel-space ratios of H1-IW1 are located below the correlation line, indicating a lesser increase in the gel-space ratio than that of the MPC system. Increasing the gel-space ratio with the increase of reaction degree supports the assumption that the compressive strength increased due to the increase of the gel-space ratio. The space is more efficiently and homogenously filled/ occupied by low-density material. It is worth mentioning that relating compressive strength to the gel-space ratio in concretes with reacting aggregate is new, especially with the support of long-term field data. Evaluating the gel-space ratio in this case comprises many challenging points, such as considering aggregate-paste reaction, which differs from thermodynamic equilibrium calculations. The analysis methods used in this section remain useful despite the scarcity of data at higher temperatures.

6 Implication for Plant Life Management

Coring data like in this study are essential for the safety assessment of nuclear power plant buildings in the long term. Within the frame of a single project, the coring samples in this study were obtained from multiple buildings of different construction ages. Chemical composition and mechanical properties were examined for each core via comprehensive experimental methods. The results enabled us to assess the time-dependent evolution of strength and chemical composition. Recordings of environmental conditions during building usage and consistent experimental conditions during sampling and testing made the results even more valuable for long-term plant life management.

The model proposed based on core data analysis can help predict material behavior over extended periods. This knowledge is also beneficial for constructing next-generation reactors using similar materials, ensuring reliable performance and safety. Moreover, the coring strategy and experimental program developed in this project can be easily applied to multiple plants for cross-comparison, offering additional benefits such as identifying common trends, optimizing maintenance schedules, and improving overall plant efficiency.

It is crucial to verify the conditions under which these insights hold true to apply them to other plants. Future analysis should account for differences in design, materials, and environmental factors. Since observed reactions cannot be permanent, ongoing research is necessary to investigate achievable reaction degrees, long-term material stability, and possible degradation mechanisms.

In the following, we propose a procedure, by extrapolating the findings of the study, to estimate strength distribution and time evolution to support the long-term operation of nuclear power plants constructed using aggregates of similar composition.

The key point is to relate compressive strength to the reaction degree. As the increase of strength is a consequence of the increase of gel-space ratio caused by the aggregate-paste reaction, an empirical relationship can be established between the increase of strength Δf and an additional reaction degree $\Delta\zeta$:

$$\Delta f = f - f_0 = B\,\Delta\zeta = B(\zeta - \zeta_0). \tag{11}$$

There are several options for both Δf and $\Delta\zeta$ based on the availability of in-situ measurement in practical applications. If coring is possible near the surface, Δf can be chosen as the increased strength with respect to the strength of cores near the surface, such as 100 mm from the surface, $f_0 = f_{100}$. Similarly, $\Delta\zeta$ can be the additional reaction degree with respect to the reaction degree of the core near the surface, $\zeta_0 = \zeta_{100}$. In case of no coring data, Δf can be evaluated as the increased strength with respect to the design strength $f_0 = f_d$, or the potential strength $f_0 = f_{d,90}$. In the latter case, the reference reaction degree can be chosen as $\zeta_0 \approx 1.6\%$ for walls without high-temperature history and $\zeta_0 \approx 2.1\%$ for walls with high-temperature history similar to BSWs and PEDEs, according to the data in Figure 11.

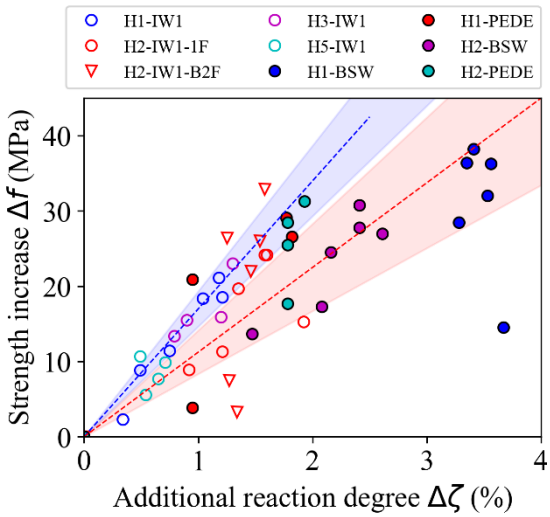

Figure 13 Relation between increase in strength and reaction degree of aggregate.

The coefficient B depends on the choice of reference strength and reaction degree and the temperature history of the walls. Figure 13 displays the correlation between strength increase Δf and additional reaction degree $\Delta\zeta$, with the strength and reaction degree of the core near the surface used as the reference values. The coefficient B was 14.7 MPa for walls without high-temperature history and 11.3 MPa for walls with high-temperature history.

In the following, we propose a methodology for applying the findings of the study to estimate concrete strength with a view to safety assessment for the aging management

of concrete structures.

Step 1: Estimate the time evolution of water content and reaction degree. Initial water content and appropriate boundary conditions are to be known. Then, five input parameters $\alpha_0, \theta, E_a, A, \beta$ of the moisture transport and reaction degree model of section 4.2 are to be decided. (4)(3)The time evolution of the reaction degree is obtained by solving Eqs. (4) and (3). Taking H5-IW1 as an example, using values for $\alpha_0, \theta, E_a, A, \beta$ from Table 7, we estimated the reaction degree evolution and showed in Figure 14a.

Step 2: Estimate strength as a function of reaction degree. The estimated time evolution of reaction degree is to be inserted into Eq.(11) to predict strength values over time. In the example of H5-IW1, we took B =14.7%. The estimated strength evolution is shown in Figure 14b. Considering deviations of experimental data from Eq.(11), prediction bands were also indicated, which correspond to the shaded area in Figure 11.

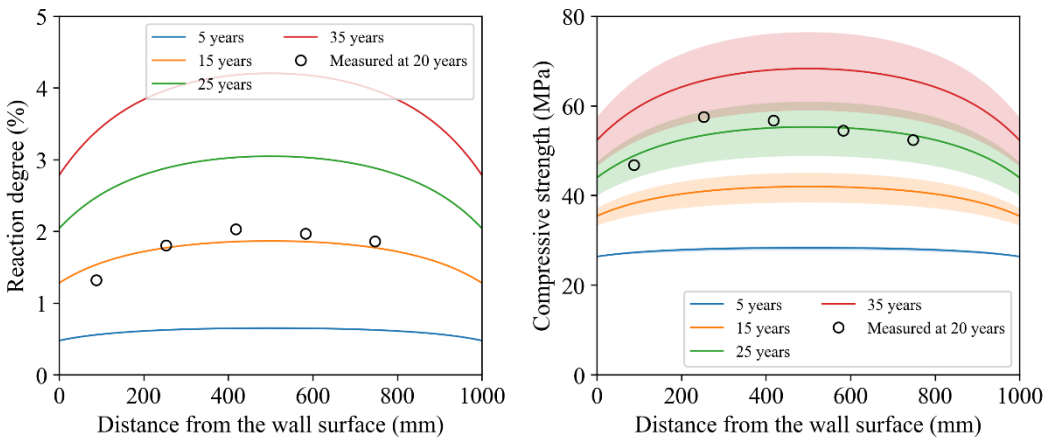

(a) (b)

Figure 14 Reaction degree (a) and strength (b) evolution over time for H5-IW1, estimated by coupled simulation of moisture-reaction combined with Eq.(11).

7 Conclusions

Cored samples were obtained from the thick concrete walls of nuclear power plants during decommissioning. These walls were aged ~50 years and constructed in different decades using aggregates from the same origin. The temperature and humidity conditions of these walls were controlled during the operation of power plants. We

found that aggregate dissolved and reacted with cement hydrates. From the time evolution of the reaction and its correlation to the compressive strength measured on cored samples, we identified that the reaction contributed to strength development. The experimental data measured on cored samples from real structures cannot be obtained in conventional laboratory experiments; they are unique in the literature and serve as an important basis to support the long-term operation of nuclear power plants.

To clarify the underlying mechanisms of strength increase, we discussed the dissolved rock-forming minerals based on the chemical composition of the reacted aggregate from ICP-AES and XRD-Rietveld analysis. The main dissolved aggregate minerals were quartz, albite, and chlorite. Albite dissolved more in later stages. The Kinetics of the reaction was studied in combination with moisture transport in concrete walls.

To promote the findings for a broader range of engineering applications, we estimated universal parameters for reaction kinetics, moisture transport, and strength increase. A protocol is proposed for the estimation of strength evolution over time in structures constructed with aggregates of similar composition. The coring methodology and experimental program, as well as the model developed in this project, can be applied to next-generation power plants constructed using similar materials to monitor performance and safety.

As a prospective improvement, accounting for the impact of pH on the aggregate-paste reaction will improve the model. At the moment, in-situ variation of pH in concrete walls is not yet accessible either by experimental technique or theoretical analysis. Another point is understanding the non-equilibrium reaction between aggregate and cement hydrates, which is currently approximated by thermodynamic equilibrium simulation using GEMS.

Acknowledgment

This project was based on a research project collaboration between the University of Tokyo, Nagoya University, and Chubu Electric Power Co. Inc. and was partially supported by the "R&D of the Safety Improvement of Nuclear Facilities" project by the Ministry of Economy, Trade and Industry of Japan. The authors thank Kajima Corporation for providing the cored samples.

Appendix

A. Porosity of the cored samples

This section presents the results of porosity measurement. The porosity is shown in Figure A1a for walls without a high-temperature history, while Figure A1b shows the results for walls with high-temperature history. As discussed in section 3.1, the porosity is approximately constant and does not show any clear trend with regard to the core position.

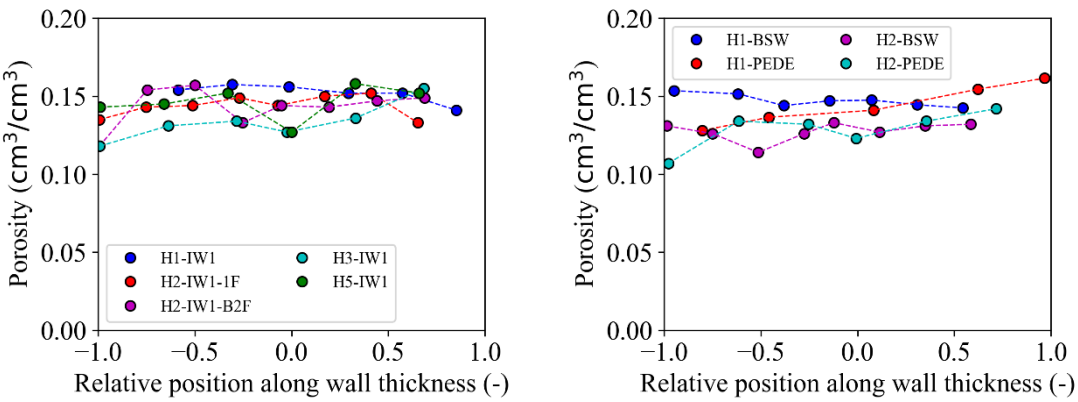

(a) (b)

Figure A1: Porosity versus position of the core along the wall thickness. X-axis 0 represents the wall center, while ±1 represents the two surfaces. (a): IW1s without high temperature history; (b): BSWs and PEDEs with high temperature history

B. Oxide composition of dissolved aggregates

This section presents the composition of dissolved aggregates for each core, obtained from Eq.(2), by comparing the oxide composition of the cement paste in cores with that of the original cement. The results are listed in Table B1.

Table B1. Oxide composition of dissolved aggregates for each core

Wall	Core position	SiO_2	Al_2O_3	Fe_2O_3	MgO	Na_2O	K_2O
H1-IW1	S-100	89.33	6.39	2.24	0.00	2.03	0.00

	S-300	89.22	6.47	2.39	0.00	1.92	0.00
	S-500	88.17	7.30	2.69	0.00	1.85	0.00
	N-700	87.40	6.80	2.55	0.00	3.24	0.00
	N-500	88.50	6.92	2.52	0.00	2.06	0.00
	N-300	89.08	6.90	2.54	0.00	1.48	0.00
	N-100	89.53	5.80	2.03	0.00	2.64	0.00
H1-BSW	W-110	68.66	5.40	2.34	0.00	11.38	12.22
	W-390	78.26	6.97	1.92	0.00	6.36	6.49
	W-640	88.12	6.06	1.46	0.00	2.70	1.66
	W-890	83.26	5.88	1.46	0.00	5.34	4.06
	W-1140	87.01	6.11	1.85	0.00	2.94	2.09
	W-1415	83.23	6.09	1.54	0.00	5.20	3.94
	W-1690	85.07	6.01	1.52	0.00	4.42	2.98
H1-PEDE	E-100	83.81	9.34	3.54	0.98	2.33	0.00
	E-300	85.44	8.36	2.76	0.56	2.89	0.00
	E-500	85.39	8.53	2.98	0.54	2.56	0.00
	E-700	84.18	8.86	2.97	0.59	3.41	0.00
	E-900	83.79	9.13	3.30	0.73	3.04	0.00
H2-IW1-1F	S-90	85.31	8.67	4.21	1.87	0.00	0.00
	S-295	85.01	9.19	3.32	1.38	1.10	0.00
	S-500	85.36	9.13	2.92	1.13	1.46	0.00
	S-705	85.86	8.47	2.57	1.54	1.56	0.00
	S-910	85.89	8.68	2.35	1.49	1.59	0.00

	S-1115	84.59	9.81	2.97	1.20	1.42	0.00
	S-1320	82.90	10.80	3.02	1.42	1.85	0.00
H2-IW1-B2F	N-90	89.04	6.53	3.95	0.91	0.00	0.00
	N-300	87.35	7.79	3.40	0.70	0.77	0.00
	N-510	87.24	8.07	2.73	0.89	1.07	0.00
	N-720	87.16	7.90	2.96	0.81	1.18	0.00
	N-930	86.97	7.92	3.13	0.82	1.15	0.00
	N-1140	86.36	8.86	2.85	0.78	1.15	0.00
	N-1350	86.81	8.17	3.17	0.89	0.96	0.00
H2-BSW	N-100	78.26	12.39	7.29	2.49	-0.43	0.00
	N-395	82.88	9.85	4.38	1.36	1.53	0.00
	N-690	82.63	9.53	4.43	1.27	2.14	0.00
	N-985	82.39	10.20	4.37	1.20	1.84	0.00
	N-1230	82.91	9.33	4.07	1.27	2.42	0.00
	N-1475	83.06	9.94	4.04	1.20	1.76	0.00
	N-1720	82.76	9.99	3.96	1.15	2.14	0.00
H2-PEDE	W-105	85.78	9.05	3.10	0.86	1.20	0.00
	W-350	86.59	8.88	2.10	0.49	1.94	0.00
	W-600	87.19	8.68	1.39	0.31	2.43	0.00
	W-850	87.45	8.71	1.26	0.18	2.41	0.00
	W-1090	87.30	8.97	1.14	0.24	2.35	0.00
H3-IW1	W-90	75.52	13.42	3.32	7.01	0.73	0.00
	W-320	79.45	12.46	1.87	4.67	1.55	0.00

	W-550	80.62	11.91	1.86	3.95	1.66	0.00
	W-780	80.44	11.85	1.67	4.10	1.94	0.00
	W-1010	79.98	12.17	1.84	4.45	1.55	0.00
H5-IW1	E-87.5	84.66	10.49	2.29	2.55	0.00	0.00
	E-252.5	88.33	9.86	0.30	1.51	0.00	0.00
	E-417.5	86.60	10.79	1.02	1.59	0.00	0.00
	E-582.5	87.45	10.30	0.67	1.58	0.00	0.00
	E-747.5	87.78	10.32	0.50	1.41	0.00	0.00

References

[1] Global Cement and Concrete Association, https://gccassociation.org/concretefuture/getting-to-net-zero/, (2024).

[2] I. Maruyama, J. Rymeš, A. Aili, S. Sawada, O. Kontani, S. Ueda, R. Shimamoto, Long-term use of modern Portland cement concrete: The impact of Al-tobermorite formation, Mater Des 198 (2021). https://doi.org/10.1016/j.matdes.2020.109297.

[3] J. Rymeš, I. Maruyama, R. Shimamoto, A. Tachibana, Y. Tanaka, S. Sawada, Y. Ichikawa, O. Kontani, Long-term material properties of a thick concrete wall exposed to ordinary environmental conditions in a nuclear reactor building: The contribution of cement hydrates and feldspar interaction, Journal of Advanced Concrete Technology 17 (2019) 195–215. https://doi.org/10.3151/jact.17.5.195.

[4] A. Aili, I. Maruyama, G. Geng, S. Umeki, K. Sumitani, S. Sawada, S. Ueda, Y. Umeki, Micro X-ray diffraction and elemental study on Al-tobermorite formation in aged modern concrete, Journal of the American Ceramic Society 105 (2022) 6924–6937. https://doi.org/10.1111/jace.18624.

[5] A. Leemann, M. Bagheri, B. Lothenbach, K. Scrivener, S. Barbotin, E. Boehm-courjault, G. Geng, R. Dähn, Z. Shi, M. Shakoorioskooie, M. Griffa, R. Zboray, P. Lura, E. Gallyamov, R. Rezakhani, J.F. Molinari, Alkali-silica reaction – a

multidisciplinary approach, RILEM Technical Letters 6 (2021) 169–187. https://doi.org/10.21809/RILEMTECHLETT.2021.151.

[6] A.C. Lasaga, CHEMICAL KINETICS OF WATER-ROCK INTERACTIONS., in: J Geophys Res, 1984: pp. 4009–4025. https://doi.org/10.1029/jb089ib06p04009.

[7] M. Heřmanská, M.J. Voigt, C. Marieni, J. Declercq, E.H. Oelkers, A comprehensive and consistent mineral dissolution rate database: Part II: Secondary silicate minerals, Chem Geol 636 (2023). https://doi.org/10.1016/j.chemgeo.2023.121632.

[8] M. Bagheri, B. Lothenbach, M. Shakoorioskooie, K. Scrivener, Effect of different ions on dissolution rates of silica and feldspars at high pH, Cem Concr Res 152 (2022). https://doi.org/10.1016/j.cemconres.2021.106644.

[9] Dove - 1994 - The Dissolution Kinetics of Quartz in Sodium Chloride Solutions at 25 Degrees to 300 Degrees C, (n.d.).

[10] P.M. Dove, N. Han, A.F. Wallace, J.J. De Yoreo, Kinetics of amorphous silica dissolution and the paradox of the silica polymorphs, Proceedings of the National Academy of Sciences 105 (2008) 9903–9908. https://doi.org/10.1073/pnas.080379810.

[11] L. Chou, R. Wollast, Study of the weathering of albite at room temperature and pressure with a fluidized bed reactor, Geochim Cosmochim Acta 48 (1984) 2205–2217.

[12] R.T. Lowson, M.C.J. Comarmond, G. Rajaratnam, P.L. Brown, The kinetics of the dissolution of chlorite as a function of pH and at 25°C, Geochim Cosmochim Acta 69 (2005) 1687–1699. https://doi.org/10.1016/j.gca.2004.09.028.

[13] C.A. Rochelle, K. Bateman, R. MacGregor, J.M. Pearce, D. Savage, P.D. Wetton, Experimental determination of chlorite dissolution rates, in: Materials Research Society Symposium - Proceedings, Materials Research Society, 1995: pp. 149–156. https://doi.org/10.1557/proc-353-149.

[14] M.M. Smith, Z. Dai, S.A. Carroll, Illite dissolution kinetics from 100 to 280 °C and pH 3 to 9, Geochim Cosmochim Acta 209 (2017) 9–23. https://doi.org/10.1016/j.gca.2017.04.005.

[15] G. Yuan, Y. Cao, H.M. Schulz, F. Hao, J. Gluyas, K. Liu, T. Yang, Y. Wang, K. Xi, F. Li, A review of feldspar alteration and its geological significance in sedimentary basins: From shallow aquifers to deep hydrocarbon reservoirs, Earth Sci Rev 191 (2019) 114–140. https://doi.org/10.1016/j.earscirev.2019.02.004.

[16] V.A. Alekseyev, L.S. Medvedeva, N.I. Prisyagina, S.S. Meshalkin, A.I. Balabin, Change in the dissolution rates of alkali feldspars as a result of secondary mineral precipitation and approach to equilibrium, Geochim Cosmochim Acta 61 (1997) 1125–142.

[17] S. Poyet, Water transport properties of virtual fractal porous media: Implications for the unsaturated transport properties of cement-based materials, Cem Concr Res 150 (2021). https://doi.org/10.1016/j.cemconres.2021.106613.

[18] H. Akita, T. Fujiwara, Y. Ozaka, Akita - 1994 - An analytical method of moisture transfer within concrete due to drying, JSCE Journal Proceedings 23 (1994) 101–110.

[19] G. Plusquellec, M.R. Geiker, J. Lindgård, J. Duchesne, B. Fournier, K. De Weerdt, Determination of the pH and the free alkali metal content in the pore solution of concrete: Review and experimental comparison, Cem Concr Res 96 (2017) 13–26. https://doi.org/10.1016/j.cemconres.2017.03.002.

[20] B. Lothenbach, T. Matschei, G. Möschner, F.P. Glasser, Thermodynamic modelling of the effect of temperature on the hydration and porosity of Portland cement, Cem Concr Res 38 (2008) 1–18. https://doi.org/10.1016/j.cemconres.2007.08.017.

[21] B. Lothenbach, D.A. Kulik, T. Matschei, M. Balonis, L. Baquerizo, B. Dilnesa, G.D. Miron, R.J. Myers, Cemdata18: A chemical thermodynamic database for hydrated Portland cements and alkali-activated materials, Cem Concr Res 115 (2019) 472–506. https://doi.org/10.1016/j.cemconres.2018.04.018.

[22] T.C. Powers, T.L. Brownyard, Studies of the Hardened Paste by Means of Specific-Volume Measurements, Portland Cement Association Bulletin (1947) 669–712.

[23] T.C. POWERS, Structure and Physical Properties of Hardened Portland Cement Paste, Journal of the American Ceramic Society 41 (1958) 1–6. https://doi.org/10.1111/j.1151-2916.1958.tb13494.x.

[24] A. Schöler, B. Lothenbach, F. Winnefeld, M. Zajac, Hydration of quaternary Portland cement blends containing blast-furnace slag, siliceous fly ash and limestone powder, Cem Concr Compos 55 (2015) 374–382. https://doi.org/10.1016/j.cemconcomp.2014.10.001.

[25] B. Pichler, C. Hellmich, J. Eberhardsteiner, J. Wasserbauer, P. Termkhajornkit, R. Barbarulo, G. Chanvillard, Effect of gel-space ratio and microstructure on strength of hydrating cementitious materials: An engineering micromechanics approach, Cem Concr Res 45 (2013) 55–68. https://doi.org/10.1016/j.cemconres.2012.10.019.

[26] I. Maruyama, G. Igarashi, Cement Reaction and Resultant Physical Properties of Cement Paste, Journal of Advanced Concrete Technology 12 (2014) 200–213. https://doi.org/10.3151/jact.12.200.

[27] P. Termkhajornkit, Q.H. Vu, R. Barbarulo, S. Daronnat, G. Chanvillard, Dependence of compressive strength on phase assemblage in cement pastes: Beyond gel-space ratio - Experimental evidence and micromechanical modeling, Cem Concr Res 56 (2014) 1–11. https://doi.org/10.1016/j.cemconres.2013.10.007.

[28] B. Lothenbach, M. Zajac, Application of thermodynamic modelling to hydrated cements, Cem Concr Res 123 (2019). https://doi.org/10.1016/j.cemconres.2019.105779.

[29] Y. Ichikawa, I. Maruyama, H. Wada, K. Yokokura, S. Ishikawa, G. Saito, Soundness evaluation method for concrete structures based on the data obtained from decommissioning Hamaoka nuclear power plant, Part 3: Investigation on core sampling method, Proceeding of Annual Conf.of AIJ Structure (2017) 1259–1260.

[30] JSA, Portland cement (JIS R5210), Tokyo, Japanese Standards Association (1973).

[31] JSA, Method of test for static modulus of elasticity of concrete (JIS A 1149), Tokyo: Japanese Standards Association (2017).

[32] A. Meawad, K. Murakami, T. Ohkubo, O. Kontani, J. Etoh, M. Do Thi, C. Aparicio, C.M. Silva, I. Maruyama, Evaluation of radiation-induced amorphization of α-quartz in concrete aggregates using Raman spectroscopy, Journal of Nuclear Materials 604 (2025) 155523. https://doi.org/10.1016/j.jnucmat.2024.155523.

[33] I. Maruyama, G. Igarashi, N. Kishi, Fundamental study on water transfer in portland cement paste, Journal of Structural and Construction Engineering 76 (2011) 1737–1744. https://doi.org/10.3130/aijs.76.1737.

[34] H. Sasano, I. Maruyama, A. Nakamura, Y. Yamamoto, M. Teshigawara, Impact of drying on structural performance of reinforced concrete shear walls, Journal of Advanced Concrete Technology 16 (2018) 210–232. https://doi.org/10.3151/jact.16.210.

[35] H. Sasano, I. Maruyama, Mechanism of drying-induced change in the physical properties of concrete: A mesoscale simulation study, Cem Concr Res 143 (2021) 106401. https://doi.org/10.1016/j.cemconres.2021.106401.

[36] H. Sasano, I. Maruyama, Investigation into the changes in the splitting tensile strength of concrete subjected to long-term drying using a three-phase mesoscale RBSM, Cem Concr Compos 148 (2024) 105462. https://doi.org/10.1016/j.cemconcomp.2024.105462.

[37] F. Soleilhet, F. Benboudjema, X. Jourdain, F. Gatuingt, Effect of transient drying on mechanical properties of concrete specimens, European Journal of Environmental and Civil Engineering 26 (2022) 6650–6669. https://doi.org/10.1080/19648189.2021.1952488.

[38] M. Lin, M. Itoh, I. Maruyama, Mechanism of Change in Splitting Tensile Strength of Concrete during Heating or Drying up to 90°C, Journal of Advanced Concrete Technology 13 (2015) 94–102. https://doi.org/10.3151/jact.13.94.

[39] I. Maruyama, H. Sasano, Y. Nishioka, G. Igarashi, Strength and Young's modulus change in concrete due to long-term drying and heating up to 90°C, Cem Concr Res 66 (2014) 48–63. https://doi.org/10.1016/j.cemconres.2014.07.016.

[40] J. Glucklich, U. Korin, Effect of Moisture Content on Strength and Strain Energy Release Rate of Cement Mortar, Journal of the American Ceramic Society 58 (1975) 517–521. https://doi.org/10.1111/j.1151-2916.1975.tb18772.x.

[41] A. Idiart, J. Bisschop, A. Caballero, P. Lura, A numerical and experimental study of aggregate-induced shrinkage cracking in cementitious composites, Cem Concr Res 42 (2012) 272–281. https://doi.org/10.1016/j.cemconres.2011.09.013.

[42] I. Yurtdas, H. Peng, N. Burlion, F. Skoczylas, Influences of water by cement ratio on mechanical properties of mortars submitted to drying, Cem Concr Res 36 (2006) 1286–1293. https://doi.org/10.1016/j.cemconres.2005.12.015.

[43] N. Burlion, F. Bourgeois, J.-F. Shao, Effects of desiccation on mechanical behaviour of concrete, Cem Concr Compos 27 (2005) 367–379. https://doi.org/10.1016/j.cemconcomp.2004.05.004.

[44] I. Yurtdas, N. Burlion, F. Skoczylas, Experimental characterisation of the drying effect on uniaxial mechanical behaviour of mortar, Mater Struct 37 (2004) 170–176. https://doi.org/10.1007/BF02481616.

[45] S.E. Pihlajavaara, A review of some of the main results of a research on the aging phenomena of concrete: Effect of moisture conditions on strength, shrinkage and creep of mature concrete, Cem Concr Res 4 (1974) 761–771. https://doi.org/10.1016/0008-8846(74)90048-9.

[46] D.A. Kulik, T. Wagner, S. V. Dmytrieva, G. Kosakowski, F.F. Hingerl, K. V. Chudnenko, U.R. Berner, GEM-Selektor geochemical modeling package: revised algorithm and GEMS3K numerical kernel for coupled simulation codes, Comput Geosci (2012). https://doi.org/10.1007/s10596-012-9310-6.

[47] T. Wagner, D.A. Kulik, F.F. Hingerl, S. V. Dmytrieva, GEM-SELEKTOR GEOCHEMICAL MODELING PACKAGE: TSolMod LIBRARY AND DATA INTERFACE FOR MULTICOMPONENT PHASE MODELS, The Canadian Mineralogist 50 (2012) 1173–1195. https://doi.org/10.3749/canmin.50.5.1173.

945

946